

The following is a preprint submitted to the journal Remote Sensing of Environment for peer review on March 14, 2022 (©2023 under the [CC-BY-NC-ND 4.0 license](#)). A revised version was accepted on January 27, 2023. The definitive version from the publisher employs the title “Dependence of ocean surface filaments on wind speed: An observational study of North Atlantic right whale habitat.” All versions seek to address:

Collocations of Gulf of St. Lawrence whale sightings and synthetic aperture radar scenes
 Quantification of a dependence of submesoscale filaments at the ocean surface on wind speed
 Consistency in linear and nonlinear components of Pearson and distance correlation
 A simple wind speed adjustment of synthetic aperture radar contrast

Towards a physical characterization of North Atlantic right whale habitat from space: Dependence of surface filaments on wind speed

Richard E. Danielson, Hui Shen, Jing Tao, and William Perrie
 Bedford Institute of Oceanography, Fisheries and Oceans Canada
 Dartmouth, Nova Scotia, Canada

Keywords: ocean current deformation, synthetic aperture radar, sea surface filaments

Abstract

Coherent filaments at the ocean surface often appear to be transient watermass boundaries, where currents converge, surfactants accumulate, and frontal structure at depth can possibly delineate enhanced biological activity in the upper water column. Spaceborne synthetic aperture radar (SAR) permits filaments to be observed at O[100-m] resolution, but extensive coherent structure is more apparent in weaker winds. A wind speed adjustment is considered for filaments (i.e., contiguous SAR contrasts) of at least 10 km in length. Measures of dependence (distance correlation and the linear and nonlinear components of Pearson correlation) are examined to identify a broad peak in the relationship between filament contrast and weak or moderate values of surface wind speed, where a variable wind speed exponent is employed to maximize these measures.

Three locations of recent North Atlantic right whale (*Eubalaena glacialis*) sightings in the Gulf of St. Lawrence are sampled between 2008 and 2020 by 324 Radarsat-2 SAR scenes and 10-m wind speed from the ERA5 reanalysis. The inverse relationship between SAR contrast magnitude and wind speed is quantified, and a reduced correlation is obtained for all three domains when SAR contrast is weighted by wind speed to the power of 0.8. A more uniform emphasis on ocean surface structure within a SAR scene, or across multiple scenes, can thus be considered in the search for hotspots of biological activity in the water column.

1 Introduction

Ecosystem modelling in the Gulf of St. Lawrence (GSL) is well suited to address the stock and supply of zooplankton *Calanus* spp., the preferred prey of the endangered North Atlantic right whale (NARW), *Eubalaena glacialis* (Plourde et al. 2019; Sorocean et al. 2019; Gavrilchuk et al. 2020; Brennan et al. 2021). For an animal the size of a grain of rice, however, one of the best known indications of its local aggregation (i.e., only dense aggregations of *Calanus* offer a net energy surplus to a right whale) is the right whale herself (Baumgartner et al. 2007). Observations of right whales suggest that mothers provide foraging patterns for their young and sensory perception is employed while feeding. In addition, Kenney et al. (2001) provide a number of hypotheses about how right whales might discover *Calanus* aggregations beyond their immediate locale.

A synthesis of *Calanus* spp. life cycle and biomass distributions in the GSL is given by Sorocean et al. (2021), who highlight the need to explore aggregation at depth, as well as transient aggregation near the surface, in regions delimited by tidal mixing and freshwater pulses, and in convergent circulations in the upper mixed layer (their Fig. 5a). Among aggregation cues in high-resolution satellite images (cf. Basedow et al. 2019; Barthelmeß et al. 2021), the interpretation of sun glitter and synthetic aperture radar (SAR) images is relatively well developed. An historical account is given by Munk et al. (2000), who address the dynamics of cyclonic eddies in which coherent filaments at the ocean surface can be seen to evolve. This submesoscale view of eddies, fronts, and internal waves is aided by the appearance of surfactants (surface active materials) on the ocean, typically following a relaxation of the wind. Surfactants may be of terrestrial or atmospheric origin, and sources in the water column can include bacteria, plankton, fish, and oil seepage (Espedal et al. 1998; Hamilton et al. 2015; Kurata et al. 2016).

Munk et al. (2000) propose that decaying boundary layer circulations provide an initial organization of surfactants into filaments, which can gather along watermass strainlines to form extensive connections (Peacock and Haller 2013; Maps et al. 2015). Dong et al. (2021) further propose that zooplankton aggregations in Norwegian shelf waters are enhanced by such transient material boundaries. Sun glitter and SAR images capture snapshots of coherent filaments moving with the upper ocean current, but an important caveat is that filaments are only observed within a maximum wind speed range of about 1-15 ms⁻¹. The lower limit is a noise floor, and at the upper limit, wind- and wave-induced roughness pat-

terns effectively mask the underlying ocean structure. Within this range, extensive filaments are more apparent in SAR images in weaker winds (e.g., Espedal et al. 1998; Munk et al. 2000).

Radar and optical modelling of the ocean surface are well suited to address a dependence on viewing and environmental conditions. Kudryavtsev et al. (2012a,b) provide a unified framework for finescale contrasts in SAR normalized radar cross section (σ_o) and sun glitter mean square slope (s^2), which for measurements are defined as

$$\frac{\sigma_o - \overline{\sigma_o}}{\overline{\sigma_o}} \quad \text{and} \quad \frac{s^2 - \overline{s^2}}{\overline{s^2}}, \quad (1)$$

respectively. The overbar denotes a smoothing to lower resolution. Kudryavtsev et al. (2012b) formulate an extension of the radar imaging model (RIM; Kudryavtsev et al. 2005) to include sun glitter contrasts. Kudryavtsev et al. (2012a) further derive an estimate of surface current convergence from satellite SST. These studies indicate that submesoscale contrasts (1) are spatially well correlated with each other and with surface current convergence. The extended RIM model provides functional expressions of SAR and sun glitter contrasts. Both vary linearly with ocean current convergence, and in weak winds, have a sensitive nonlinear dependence on surfactants (e.g., in terms of thickness or elasticity). Regarding wind speed, sun glitter varies linearly with the inverse of friction velocity, whereas SAR is generally more sensitive and nonlinear, or almost linearly varying with the inverse of friction velocity squared (Kudryavtsev et al. 2012b).

The functional form of the RIM model suggests that wind stress and surface current convergence can be considered somewhat independently of their prior coupled evolution. In other words, a SAR snapshot might capture a similar transient pattern of ocean current contrasts in stronger or weaker winds, except that the contrasts themselves are weaker or stronger, respectively. It is then possible to consider an adjustment that offers more uniformity in filament contrast, both within an individual SAR scene and for as many GSL scenes as are available. Following Kenney et al. (2001) and Sorocean et al. (2021), this semblance of uniformity may be helpful for building hypotheses about the location of transient *Calanus* aggregations. Adjusted SAR contrasts can be interpreted preferentially in terms of ocean current convergence, or perhaps more accurately, as *current deformation* by a combination of convergence and strain (Raschle et al. 2014). Hence, our search for *Calanus* would begin by building on this assumption as well.

We introduce measurement modelling as well suited to assess the performance of a SAR con-

trast adjustment on wind speed, even though a dependence on sea state (and other variables) is expected. In this study, correlation measures are employed to summarize measurement dependence (Edelmann et al. 2021). Following Székely and Rizzo (2009) and Danielson et al. (2020), an attempt is made to separate linear and nonlinear components of the relationship between SAR contrast and wind speed. Our assessment can be considered *specific* to the choice of GSL measurements. By comparison, the RIM model (Kudryavtsev et al. 2012b) targets a *general* expression (i.e., consistent with a broader set of measurements) of the SAR contrast and friction velocity relationship. We thus propose to con-

firm a partial, and therefore nonlinear, relationship by measurements that focus on right whale foraging habitat and on filaments that are identified as contiguous SAR contrasts (cf. Young et al. 2008). Section 3 describes an identification of filaments and our dependence measures, with autocorrelation assumptions given in the Appendix. The relationship between contiguous contrasts and wind speed is examined in Section 4, where an adjustment is applied. Conclusions are given in Section 5. The next section describes right whale sightings for 2015-2020, SAR and wind data for 2008-2020, and three subdomains of interest in the GSL.

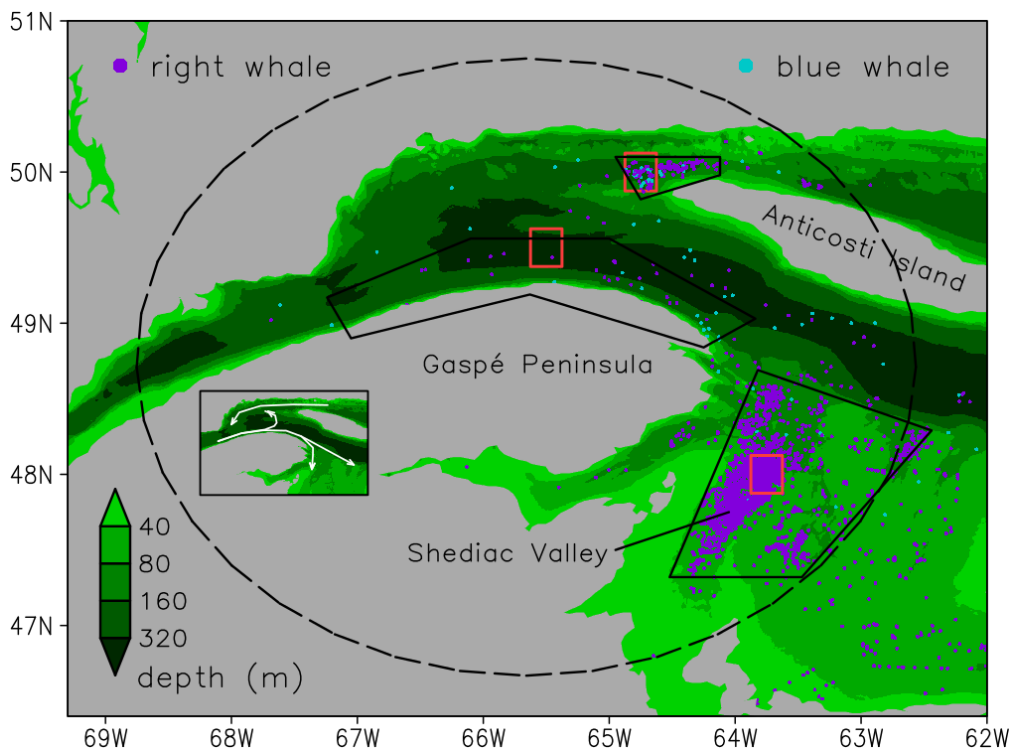


Figure 1: Location of 4986 visual sightings of the North Atlantic right whale (*Eubalaena glacialis*; purple dots) and blue whale (*Balaenoptera musculus*; blue dots) between 2015 and 2020, along with bathymetry (green shading) of the western Gulf of St. Lawrence. Solid black lines encompass the Anticosti (northern), Gaspé (western), and Shediac (southern) domains (see text). Red lines encompass the corresponding ERA5 10-m wind speed gridboxes. White arrows in the inset show the circulation pattern of the western Gulf. Radarsat-2 SAR acquisitions are initially identified as those that overlap with the dashed circle.

2 Data

A significant shift in prey availability in the 2010s (Sorocean et al. 2019) seems to have led the extant NARW population away from their traditional foraging habitats in the Gulf of Maine and Scotian Shelf and toward shallower regions of the Gulf of St.

Lawrence (GSL), where they were sighted only occasionally prior to 2013 (Kenney 2019). Since 2015, NARWs have been sighted between May and November, more frequently along the Shediac Valley in the southwestern GSL, and (with a few sightings of blue whales) in a small region just northwest of Anticosti Island (Fig. 1). As part of a broad cyclonic circu-

lation in the Gulf (Koutitonsky and Bugden 1991; Lavoie et al. 2016), the Anticosti sightings are furthest upstream (northern domain in Fig. 1) and flow is generally westward along the north shore until it merges with the Gaspé Current (elongated western domain). The relatively fresh St. Lawrence estuary outflow also feeds this coastal current, as it flows around the Gaspé Peninsula. The Gaspé Current is known to transport *Calanus* spp., with periodic intrusions onto the Shediac Valley (the southern domain; Brennan et al. 2021). The 2019 warm season is notable for having high St. Lawrence river runoff and good SAR coverage.

2.1 Whale Sightings

This study employs whale sightings from two sources. The North Atlantic Right Whale Consortium (NARWC) sightings database (Kenney 2019; NARWC 2021) includes 3277 aerial survey and vessel-of-opportunity right and blue whale sightings (either of a whale group or an individual whale) from 2015 onward in the GSL. A complementary Fisheries and Oceans Canada (DFO) database contains 2660 sight-

ings of right and blue whales (DFO 2020). Some DFO sightings might have been of dead whales, but this is only recorded in the NARWC data (which reduces the NARWC data from 3277 to 3200). As the DFO sightings are reported in local time, 4 h are added to be consistent with NARWC sightings in UTC.

The NARWC and DFO datasets each contain identical sightings separated by only a few minutes and less than a kilometer. This highlights that the same observer, or multiple observers, may report on the same whale more than once (and that selected whales are counted more often than others, either on the same day or on different days). This observing-effort duplication is retained. Unrelated to effort, the NARWC and DFO sightings are also partially overlapping, so duplicates are omitted if two sightings of the same number of right or blue whales occurs within 24 h and 0.01° latitude and longitude. This reduces the combined number of sightings by 874. For the remaining 4986 sightings (1786 and 3200; Fig. 1), there are 4900 sightings of right whales as a group or individual (7591 sightings as individuals). The counts per year are listed in Table 1, with the caveat that 2019 and 2020 sightings are preliminary.

Year	NARW Sightings	SAR Scenes	Scenes with NARWs	Sightings in Scenes
2015	114/343	86	2 (2%)	2/3 (2%/1%)
2016	100/159	53	3 (6%)	6/9 (6%/6%)
2017	1151/2118	83	11 (13%)	165/278 (14%/13%)
2018	1622/2913	105	4 (4%)	31/33 (2%/1%)
2019	1904/2049	188	31 (16%)	669/705 (35%/34%)
2020	9/9	68	0 (0%)	0/0 (0%/0%)

Table 1: Number of Gulf of St. Lawrence NARW sightings (by group/individual), and SAR scenes per year between 2015 and 2020 (the 2019 and 2020 sightings are preliminary). Included are the number of scenes with right whales, and the number of right whale sightings (by group/individual) collocated with those scenes, with fractions of their total in brackets. A sighting is considered to be temporally collocated with a SAR scene if both occur on the same day. Coverage by SAR (of dashed circle in Fig. 1) is from May to December and includes 11 (2008), 24 (2009), 31 (2010), 99 (2011), 63 (2012), 68 (2013), and 62 (2014) scenes prior to 2015.

2.2 Synthetic Aperture Radar (SAR)

The Radarsat-2 C-band (5.3-cm) SAR has been operating since May 2008 in a polar orbit about 800 km above the surface. It has a pixel resolution of 100 m or smaller, over swaths of more than 300 km, and is capable of transmitting and receiving in horizontal and vertical (H and V) polarization at incidence angles between 20° (near range) and 49° (far range). We consider all acquisitions during the months of May through December of 2008-2020 that overlap with the dashed circle in Fig. 1. This yields 941 SAR scenes that transmit and receive using the same polarization

(i.e., HH or VV), and all but three employ a narrow or wide ScanSAR beam mode. Although SAR coverage of the GSL varies somewhat by year (Table 1), sightings coverage is notable in 2017 and 2019, with 2019 having the most sightings (1904), the best GSL coverage (188 scenes), and the best sightings coverage (35%).

We also focus on a subset of scenes that provide coverage of the Anticosti, Gaspé, and Shediac domains between mid-May and mid-August (i.e., when whales are foraging, but winds are weak and filaments are easier to identify). This subset has 177, 241, and 237 scenes, respectively (a total of 324 scenes). Ini-

tial SAR processing involves reducing the resolution of normalized radar cross section (σ_o) by a smoothing operator that halves resolution on each pass (Koch 2004). This yields scenes at 100-m, 200-m, 400-m, 800-m, 1600-m, 3200-m, 6400-m, and 12800-m resolution (e.g., Fig. 2a,g,l). At 800-m resolution, we also mask σ_o using the CMOD5 VV ocean wind model (Hersbach et al. 2007), with the incidence-angle polarization ratio of Zhang et al. (2011) for HH scenes.

This permits a restriction on wind speed to $1\text{--}15\text{ ms}^{-1}$ when identifying filaments (Espedal et al. 1998; Munk et al. 2000), where a conservative bound on σ_o is imposed by assuming a wind direction toward the satellite if σ_o is small, and a wind direction parallel to the satellite track if σ_o is large. (A surface wind analysis would provide a nearly equivalent, but perhaps slightly smoother, wind speed mask.)

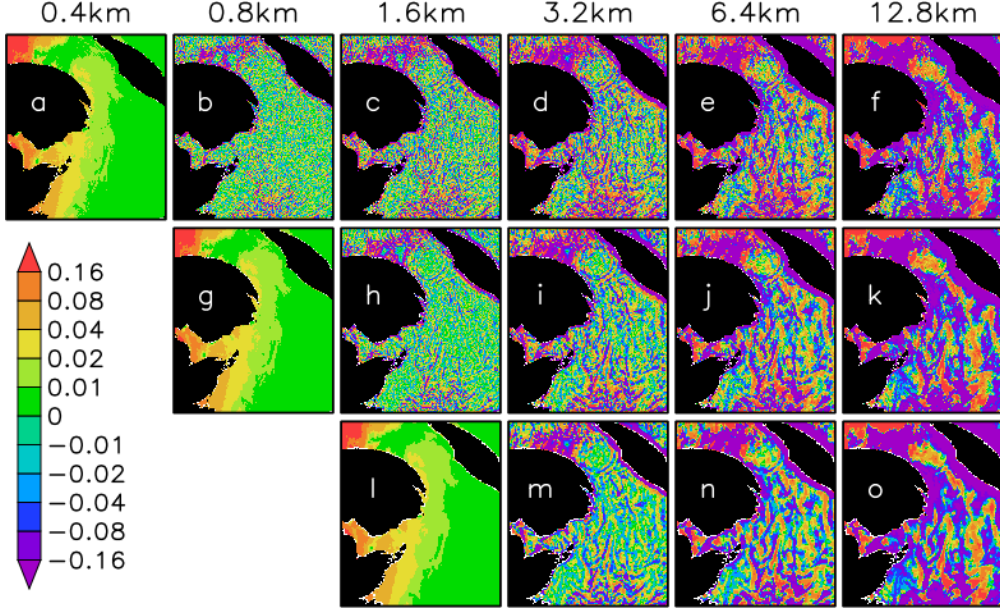


Figure 2: Normalized radar cross section (σ_o) and SAR contrast (1) at different pixel resolutions for a Radarsat-2 scene (HH) acquired over the Gulf of St. Lawrence on July 26, 2019 (21:59 UTC). Shown are σ_o at a) 0.4-km resolution and contrast at scales up to b) 0.8 km, c) 1.6-km, d) 3.2-km, e) 6.4-km, and f) 12.8-km resolution. Similarly, σ_o is shown at g) 0.8 km with contrast to h-k) 1.6-km through 12.8-km resolution, and at l) 1.6-km with contrast to m-o) 3.2-km through 12.8-km resolution, respectively. Values are in linear units with a colourbar on the left.

2.3 Surface Wind Analysis

Zonal and meridional wind analyses at 10 m above the surface are taken from the fifth European Centre for Medium-Range Weather Forecasting Reanalysis (ERA5; Hersbach et al. 2020). This reanalysis employs a spectral atmospheric forecast model and a sequential data assimilation system with 137 vertical levels and an effective horizontal resolution of 31 km. The four-dimensional variational (4D-Var) analysis is performed over successive 12-h periods. Bias adjustment of selected observations accommodates systematic differences between the model and observations (Dee 2005). The global atmosphere, land surface, and ocean surface wave evolution is given at hourly intervals from 1950 onward. Wind analyses are obtained from an archive that is resampled at 0.25° , and three

sampled locations (red boxes in Fig. 1) are taken as representative ERA5 surface wind estimates for the Anticosti, Gaspé, and Shediac domains.

3 Methods

Extensive dynamical connections can be found in SAR and sun glitter contrast patterns collected over most of the world’s oceans (Munk et al. 2000). Observations and models motivate a wind speed adjustment, but here, we seek an adjustment that is specific to our choice of two measurements (i.e., coherent SAR contrasts and ERA5 wind speed in the Fig. 1 domains). First, we confirm that contrast magnitude depends on wind speed. Next, because this partial relationship is expected to be nonlinear (e.g.,

Kudryavtsev et al. 2012b), we gauge a dependence on wind speed to some power. The power that yields the strongest dependence is taken as appropriate. Our experimental design and proposed adjustment rely on

a) an identification of coherent SAR contrasts, and b) measures of the strength of their wind speed dependence.

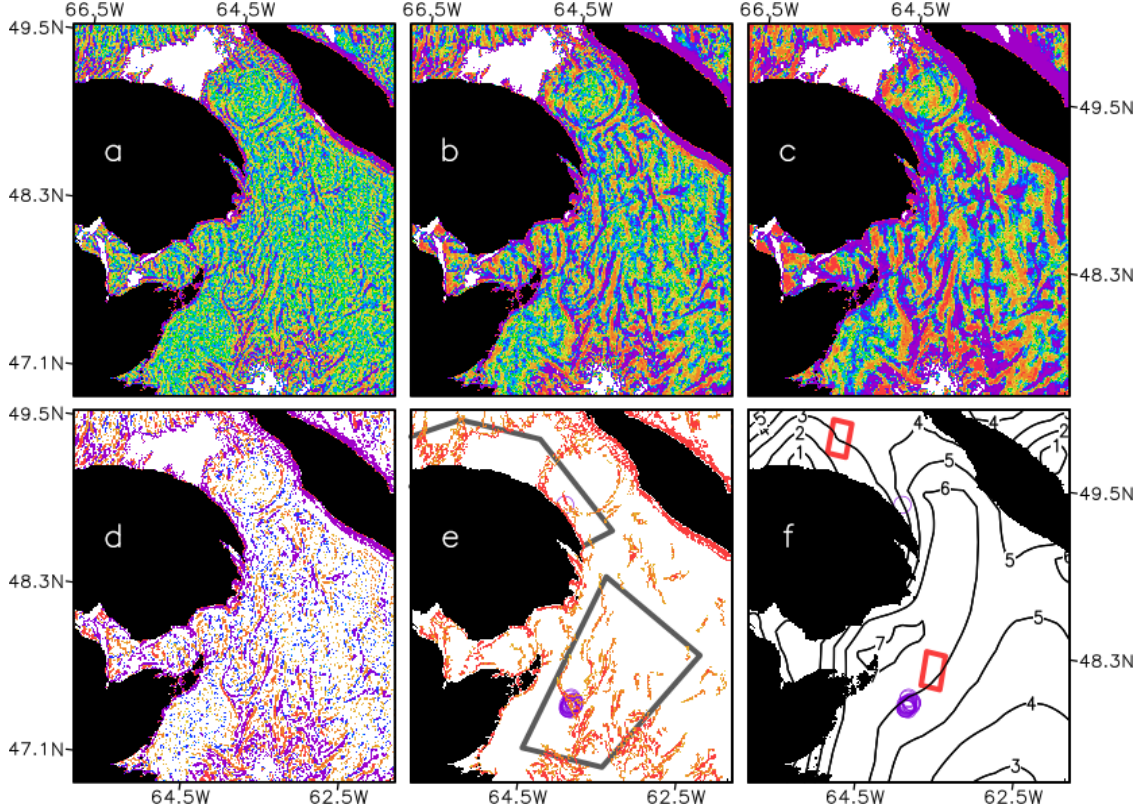


Figure 3: Filament processing and ERA5 wind speed, starting with a,b,c) Fig. 2h,i,j, but including SAR wind speed masking (see text). Also shown are d) an average of (a,b,c) for contrast values of the same sign that are greater than 0.3 in magnitude, e) contrast magnitude for filaments defined by the contiguous values of (d) that cover a distance of at least 10 km [see Fig. 2 colourbar for (a-e)], and f) ERA5 10-m wind speed at 1-ms^{-1} intervals. Included in (e) and (f) are right whale sightings on this day (purple circles), and the e) SAR (grey) and f) ERA5 (red) domains of Fig. 1.

3.1 Filament Coherence

Although 286 (88%) of the 324 GSL SAR scenes employ VV polarization, a separate HH wind speed adjustment is not considered here because local SAR measurement contrast (1) is given as an HH or VV ratio. We take coherence to be contiguous contrasts that span a distance of at least 10 km. Following Kudryavtsev et al. (2012b), σ_o and $\overline{\sigma_o}$ can be averages over moving windows of, say, 250-m and 25-km respectively. Although such boxcar averages can include a wide range of finescale structure (i.e., roughly equivalent to the scales between our 100-m and 6.4-km nominal pixel resolutions; Koch 2004), an initial examination of a range of resolution brackets helps

to determine the shape and extent of the filaments of interest.

There are 28 possible combinations of σ_o and $\overline{\sigma_o}$ for resolutions between 100 m and 12800 m. A subset of 12 combinations is shown in Fig. 2 for a SAR scene acquired on July 26, 2019. As expected, large scale contrast patterns vary mainly with $\overline{\sigma_o}$, so column panels are similar. However, $\overline{\sigma_o}$ at 800-m (Fig. 2b) and 12800-m (Fig. 2f,k,o) resolution seem to capture not enough or too much of this large scale pattern, respectively. Instead, we opt to define filaments where there is agreement in contrast among, for example, Fig. 3a,b,c. That is, we consider σ_o at 800-m, and $\overline{\sigma_o}$ at 1600-m, 3200-m, or 6400-m pixel resolution. By agreement, we mean an average of these three con-

trast values, but only where all are positive or negative and larger in magnitude than 0.3. This agreement among three overlapping resolution brackets serves to isolate contiguous contrasts (Fig. 3d), from which filaments are identified that span a distance of at least 10 km (Fig. 3e). To compare with representative values of ERA5 wind speed (Fig. 3f red boxes), we obtain a single value of contrast magnitude for each of the three GSL domains by averaging on the overlap with each SAR scene. Because overlap values are set to zero outside filaments, it is only the values inside filaments that make a nonzero contribution to domain averages.

Figure 3 helps to motivate an adjustment for wind speed across a single SAR scene. Twenty-one right whale sightings are clustered in Fig. 3e (purple circles) along filaments that appear to bound a southward intrusion of the Gaspé Current into the Shediac domain. Further upstream, between the Gaspé Peninsula and Anticosti Island is the signature of a large anticyclonic excursion of the Gaspé Current (i.e., an Altika pass on this day indicates a positive sea surface height anomaly; not shown). The anticyclonic excursion and Shediac intrusion are collocated with relatively strong wind speed (Fig. 3f) and are weakly delimited by filaments. On the other hand, further south of the whales is a cyclonic eddy surrounded by extensive filaments that are partially masked (Fig. 3a,b,c). Similarly, part of the Gaspé domain is masked where wind speed is weak. Although filaments are extensive where σ_o is close to the Radarsat-2 noise floor, the search for *Calanus* is more interesting in the presence of whales (Kennedy et al. 2001; Baumgartner et al. 2007). In this case, an adjustment that emphasizes the contrasts in strong wind, relative to contrasts in weak wind, seems reasonable.

3.2 Dependence Measures

Székely et al. (2007) and Székely and Rizzo (2009) formulate a measure of dependence called distance correlation that is sensitive to nonlinear and non-monotone measurement covariance, and thus extends and complements Pearson correlation. Whereas Pearson correlation is known mainly as a measure of linear dependence, it is also possible to formulate a wavelike measurement model that accommodates both linear and nonlinear dependence (Danielson et al. 2018, 2020). As noted in the Appendix, autocorrelation provides a basis for wavelike model solutions. For SAR contrast magnitude (C) and ERA5 wind speed (U) in the domains of Fig. 1, the model,

variance, and cross-covariance components are

$$\begin{aligned} C &= t + \epsilon + \epsilon_C \\ U &= \alpha_U + \beta_U t + \epsilon + \epsilon_U \\ \text{Var}(C) &= \sigma_t^2 + \sigma_\epsilon^2 + \sigma_C^2 \\ \text{Var}(U) &= \beta_U^2 \sigma_t^2 + \sigma_\epsilon^2 + \sigma_U^2 \\ \text{Cov}(C, U) &= \beta_U \sigma_t^2 + \sigma_\epsilon^2. \end{aligned} \quad (2)$$

This model introduces linear association (t), nonlinear association (ϵ), and a lack of association (ϵ_C and ϵ_U) as signal-and-noise terms (but whose interpretation is based on signal), with variance σ_t^2 , σ_ϵ^2 , and σ_C^2 and σ_U^2 , respectively. Such a framework can be said to relate measurements with each other, but only by way of what they both measure (Danielson 2021). Thus, $t + \epsilon$ (in C) and $\alpha_U + \beta_U t + \epsilon$ (in U) capture the total association between C and U , where α_U and β_U are, respectively, an additive and multiplicative calibration of t in U .

Dependence of SAR contrast magnitude (C) on ERA5 wind speed (U) can be measured using both Pearson and distance correlation. A novel decomposition of Pearson correlation [$\rho = \text{Cov}(C, U) / \sqrt{\text{Var}(C)\text{Var}(U)}$] is also permitted by the linear ($\beta_U \sigma_t^2$) and nonlinear (σ_ϵ^2) components of $\text{Cov}(C, U)$. Multiple solutions of each component are given below, based on samples of ERA5 wind speed at intervals from 1 h to 5 h (cf. Appendix). The two key parameters required to solve (2) are β_U and σ_t^2 , and for smooth solutions, it is convenient to fix one of these. Although Danielson et al. (2018) fix β_U , here we fix σ_t^2 to the reverse linear regression value of $\text{Cov}^2(C, U) / \text{Var}(U)$.

Dependence within each domain of Fig. 1 is examined by correlating C and U^x , where x is a variable exponent in the range $[-5, 5]$. The value x^* that yields the strongest correlation is then taken as an appropriate wind speed adjustment. Because the relationship is inverted (e.g., strong contrast tends to occur in weak winds), we multiply each of three SAR contrast values by $(V/6)^{x^*}$, where V is wind speed interpolated across the scene (i.e., applied to contrast at 800-m, with $\bar{\sigma}_o$ at 1600-m, 3200-m, and 6400-m pixel resolution, including outside the domains of Fig. 1). Also, because neither Pearson nor distance correlation depend on a multiplicative calibration of C (Székely et al. 2007), we include the arbitrary normalization $(1/6)^{x^*}$ as part of this adjustment, so contrast values at wind speeds of 6 ms^{-1} are unchanged.

4 Results

Right whale foraging in the GSL can extend into the fall (NARWC 2021; DFO 2020), but we focus on SAR scenes during mid-May to mid-August, when winds

are lighter and *Calanus* near the surface may be more dense (Brennan et al. 2021; Sorocean et al. 2021). It is easier to pick out a dependence on ERA5 wind speed in the seasonal averages (Fig. 4c,d) than the individual overpasses (Fig. 4a,b). For example, during years of good SAR coverage, wind speed in the Shediac domain tends to be larger (red dots in Fig. 4d) and contrast magnitude smaller (Fig. 4c) than in other domains. As expected, Pearson correlation is uniformly negative. Distance correlation, which only

takes on values between zero and one (i.e., where zero indicates independence), is slightly smaller in the Gaspé domain, perhaps in part because its ERA5 gridbox is less representative of wind speed throughout the corresponding SAR domain (Fig. 1). Nevertheless, Pearson and distance correlation both seem consistent with observations (Espedal et al. 1998; Munk et al. 2000) and model predictions (Kudryavtsev et al. 2012a,b) of a filament contrast dependence on wind speed.

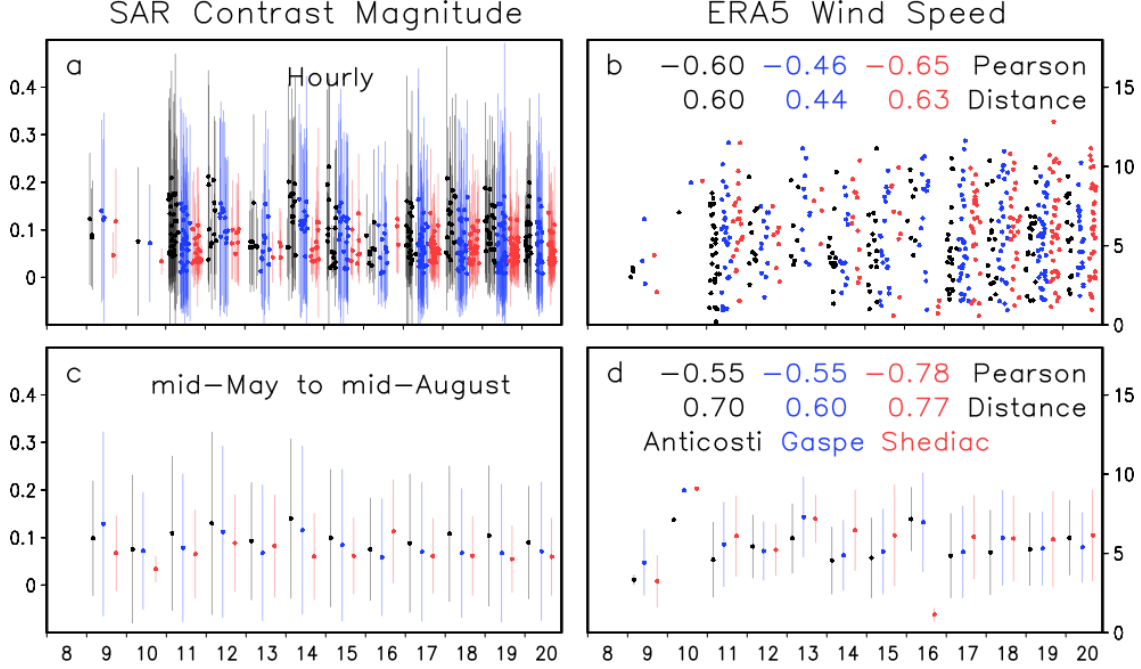


Figure 4: Mid-May to mid-August values of a,c) SAR contrast magnitude (C) and b,d) ERA5 wind speed (U) during 2008-2020 for the Anticosti (black), Gaspé (blue), and Shediac (red) domains of Fig. 1. The Anticosti and Shediac values are shifted by 3.5 months earlier and later, respectively. Shown are averages a,b) for each domain overpass (hourly interval) and c,d) for all overpasses between mid-May and mid-August (annual interval; dots with lines above and below of one standard deviation), and the corresponding Pearson and distance correlation values for each domain and time interval. The abscissa is year since 2000.

Figure 5 depicts (C, U^x) correlation magnitude as a function of wind speed exponent (x) for the hourly SAR and ERA5 data of Fig. 4a,b. Across all exponents, distance correlation seems more similar in value (i.e., flatter) than the Pearson correlation. Most correlation minima occur at large negative exponents. Maxima in Pearson and distance correlation (filled circles) are similar to the tabulated values of Fig. 4b (at an exponent of one), but typically occur at an exponent of less than one. At least for the Gaspé and Shediac domains, maxima in Pearson correlation exceed that of distance correlation to a degree expected of bivariate normal data (Székely et al. 2007,

their Fig. 1). This is consistent with small skewness of the U^x distributions for x in the range $[0, 2]$ (not shown).

Away from their maxima, distance correlation is larger in magnitude than Pearson correlation, which seems consistent with a greater sensitivity to nonlinear and nonmonotonic dependence (Székely et al. 2007). Solutions of (2) at fixed σ_t^2 are not always available, but where there is a nonlinear contribution to Pearson correlation (filled diamonds), the larger value of distance correlation also suggests a nonlinear dependence. Pearson and distance correlation thus seem quite consistent in this study. Both suggest a

wind speed adjustment by an exponent of slightly less than one, which is close to the dominant linear dependence, but is shifted slightly toward a secondary nonlinear dependence (at an exponent of between -0.5 and -2). Also notable is that the linear and nonlinear

correlation maxima of Fig. 5 are not directly comparable to the SAR contrast formulae of Kudryavtsev et al. (2012b), but the use of friction velocity instead of wind speed might facilitate a more direct comparison.

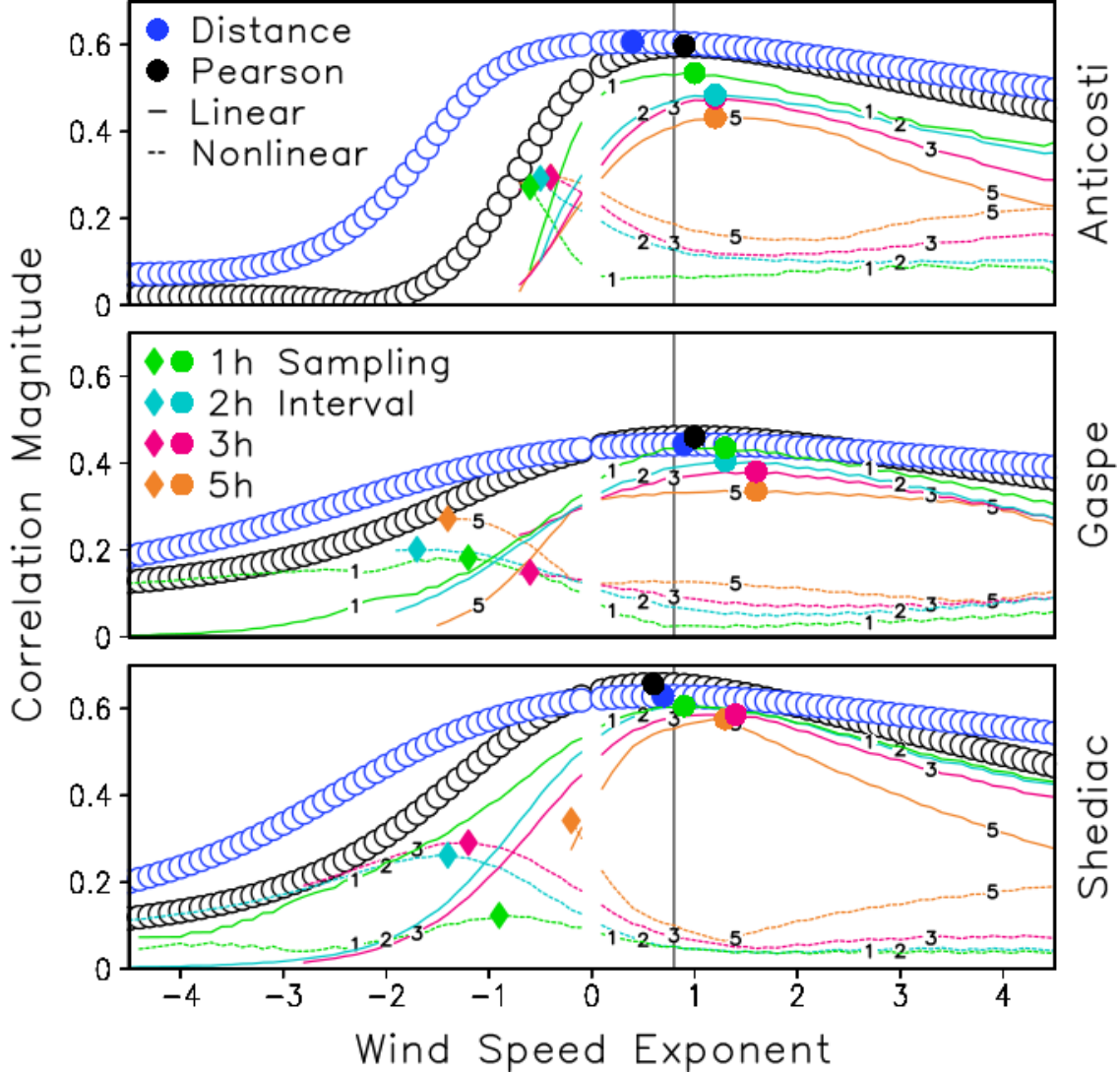


Figure 5: Dependence of Radarsat-2 SAR contrast magnitude (C) on ERA5 wind speed (U^x) as a function of wind speed exponent (x , abscissa) for the Anticosti (top), Gaspé (middle), and Shediac (bottom) domains. Shown are the magnitude of distance correlation (blue circles) and Pearson correlation (black circles), with linear (solid lines) and nonlinear (dashed lines) components of Pearson correlation based on solutions of (2) that employ four additional samples of ERA5 wind speed at 1-h (green), 2-h (cyan), 3-h (magenta), and 5-h (orange) intervals. Filled circles and diamonds are maximum values. Excluded are values at zero exponent and any component solutions that are unavailable. The vertical line at $x = 0.8$ marks a proposed adjustment.

The vertical line at $x = 0.8$ in Fig. 5 provides a compromise for the three GSL domains. We multiply SAR contrast by $(V/6)^{0.8}$ to obtain an enhance-

ment or damping, according to whether the ERA5 wind speed collocation (V) is greater than or less than 6 ms^{-1} , respectively. This is done prior to an

identification of coherent filaments (Section 3.1) and yields a reduction in the mean and variance of SAR contrast magnitude (Fig. 6a,c). Whereas Pearson and distance correlation are reduced to values of less than 0.2 (Figure 6b), exponent values greater than 0.8 do not yield a similarly reduced correlation (not shown). This suggests that our adjustment yields a reduction mainly in linear dependence, but also to some extent in nonlinear dependence. For the scene on July 26, 2019 (Fig. 7), filaments oriented along the southward

intrusion of the Gaspé Current into the Shediac domain, while small, also become more numerous. (A favourable reduction in weak wind contrast at the scene borders is also apparent.) In this case, what appear to be the transient watermass boundaries of interest are largely unchanged, but the orientation of the filaments that mark these boundaries is easier to identify. Although SAR contrast variance is still large (Fig. 6a,b), a simple adjustment provides more uniformity across individual scenes.

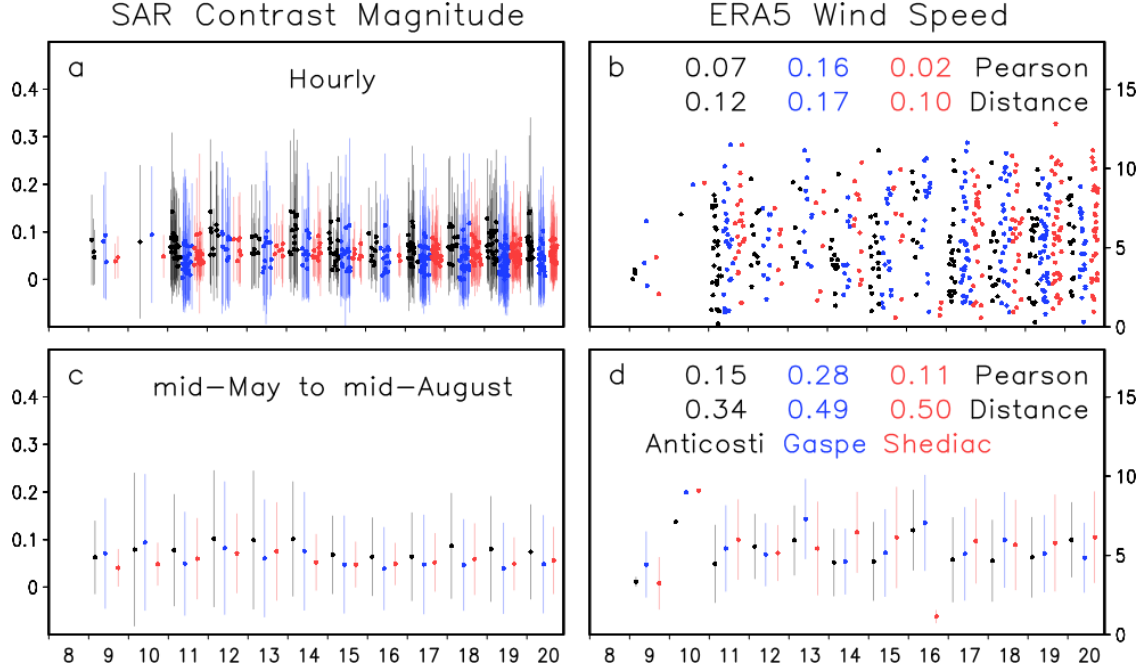


Figure 6: As in Fig. 4, but following an adjustment of SAR contrast magnitude.

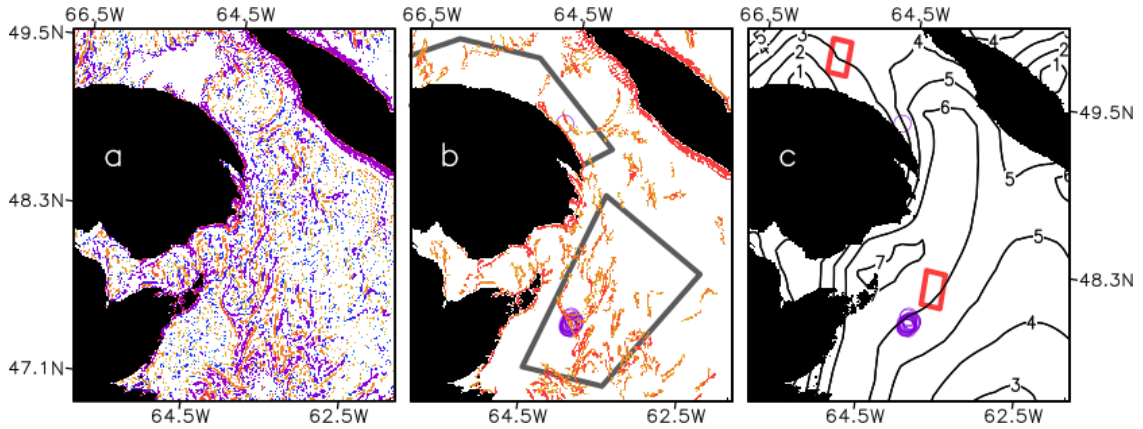


Figure 7: As in Fig. 3d,e,f, but following an adjustment of SAR contrast magnitude.

5 Conclusions

Predictions of foraging by the North Atlantic right whale (NARW) are expected to require improved familiarity with prey aggregation mechanisms at the surface and at depth (Sorocean et al. 2021). The NARW remains among the best indications of high *Calanus* concentrations, but in Gulf of St. Lawrence (GSL), can we also say that prey aggregation mechanisms are an indication of NARWs? To address the identity of such mechanisms, an exploration of surface current deformation by SAR contrast seems well motivated (Kudryavtsev et al. 2012a; Rascle et al. 2014). However, observations and models predict an inverse dependence of SAR contrast on wind forcing and sea state, at least for wind speeds within a range of $1\text{--}15\text{ ms}^{-1}$ (Espedal et al. 1998; Munk et al. 2000; Kudryavtsev et al. 2012b). In the Shediac Valley, for example, where NARWs have been sighted most frequently during 2015–2019, SAR contrast was found to be weak and wind speed strong relative to other GSL regions (Fig. 4c,d).

Radarsat-2 SAR coverage of the western GSL was found to exceed 50 scenes per year since 2011, with a maximum in 2019 of 188 scenes, which captured a third of the whale sightings that year. A focus on 324 scenes from mid-May to mid-August (2008–2020) permitted a characterization of the SAR–wind relationship when winds are lighter and *Calanus* near the surface may have been more dense. Our definition of SAR measurement contrast followed Kudryavtsev et al. (2012b), but employed agreement among three overlapping resolution brackets to isolate contiguous contrasts. Those that spanned a distance of at least 10 km contributed to an average value of contrast magnitude on the overlap with the Anticosti, Gaspé, or Shediac domains (Fig. 1). Surface wind speed at the same hour was taken from a single representative ERA5 gridpoint, which facilitated measurement model solutions that employed samples at adjacent hours (cf. Appendix).

Measurement modelling was introduced as a complement to radar imaging (and ecosystem) models that are consistent with a broader set of measurements, or that provide a general expression of SAR contrast at the air–sea interface (Kudryavtsev et al. 2012a; Rascle et al. 2014). This study focused on the strength of the relationship between SAR contrast magnitude and ERA5 wind speed to some power, using Pearson and distance correlation (Székely et al. 2007; Székely and Rizzo 2009). Because distance correlation is sensitive to nonlinear and nonmonotonic dependence, it is more consistent with general expressions of SAR contrast (e.g., including sea state and wind direction). However, both nonlinear asso-

ciation and a lack of association were also considered in (2), along with linear and nonlinear components of Pearson correlation.

Correlation magnitude was greatest for wind speed to the power of just less than one (Fig. 5) and Pearson and distance correlation were consistent. Both were close to the dominant linear dependence, but were shifted slightly toward a secondary nonlinear dependence that was apparent by the nonlinear contribution to Pearson correlation, and by a relatively large value of distance correlation. This provided a simple weighting of SAR contrast whose impact was a correlation of less than 0.2 for all GSL subdomains (Fig. 6). By making contrast magnitude more uniform (or less dependent on wind speed), filamentary contrasts along the Gaspé Current were highlighted in one scene (Fig. 7). As a basis for exploring NARW prey aggregation in a collection of SAR scenes, a simple wind speed adjustment of SAR contrast can thus be considered.

Acknowledgements

We thank the North Atlantic Right Whale Consortium and Team Whale of Fisheries and Oceans Canada for their efforts in collecting and quality controlling the GSL whale sightings. Radarsat-2 data were produced by MacDonald, Dettwiler and Associates Ltd. and obtained from the Earth Observation Data Management System of Natural Resources Canada. The ERA5 data were obtained from the Copernicus Climate Change Service (C3S) Climate Data Store. We thank M. Rizzo and G. Székely for providing the distance correlation R package (energy). Funding was provided by the Competitive Science Research Fund (CSRF) and Species at Risk (also denoted SAR) Program of Fisheries and Oceans Canada.

Appendix

Székely and Rizzo (2009) note that a separation of distance correlation into linear and nonlinear components is desirable. Because autocorrelation pertains to the solution of (2), which yields this separation in Pearson correlation, a few comments seem relevant. All correlation values in Figs. 4–6 are obtained under two temporal autocorrelation assumptions: beyond 12 h it is weak (more reasonable for SAR contrast than for ERA5 wind speed) and within 12 h it is strong (more reasonable for ERA5 wind speed than SAR contrast). The first assumption permits the use of standard correlation calculations, where it is convenient to treat each timeseries sample as independent.

(We note that a few SAR scenes are acquired within 12 h of each other in each domain of Fig. 4, but most scenes are well separated.)

The second assumption is the basis for solutions of (2), by sampling ERA5 wind speed twice before and after each SAR overpass. As in Danielson et al. (2018), a wavelike measurement model can be writ-

ten involving autocorrelated samples (i.e., where the autocorrelation is wavelike). For sampling intervals of 1 h to 5 h, the outer samples are, respectively, 2 h and 10 h before and after. The hourly ERA5 data thus permit solutions of (2), and their autocorrelation over 12 h is more robust, so this assumption also seems reasonable.

References

- Barthelmeß, T., Schütte, F., Engel, A., 2021. Variability of the sea surface microlayer across a filament’s edge and potential influences on gas exchange. *Front. Mar. Sci.* 8, 1–21, doi:10.3389/fmars.2021.718384.
- Basedow, S. L., McKee, D., Lefering, I., Gislason, A., Daase, M., Trudnowska, E., Egeland, E. S., Choquet, M., Falk-Petersen, S., 2019. Remote sensing of zooplankton swarms. *Sci. Rep.* 9, 1–10, doi:10.1038/s41598-018-37129-x.
- Baumgartner, M. F., Mayo, C. A., Kenney, R. D., 2007. Enormous carnivores, microscopic food, and a restaurant that’s hard to find, *The Urban Whale, North Atlantic Right Whales at the Crossroads*, S. D. Kraus and R. M. Rolland, Eds., Harvard University Press, 138–171, doi:10.2307/j.ctv1pnc1q9.10.
- Brennan, C. E., Maps, F., Gentleman, W. C., Lavoie, D., Chassé, J., Plourde, S., Johnson, C. L., 2021. Ocean circulation changes drive shifts in *Calanus* abundance in North Atlantic right whale foraging habitat: A model comparison of cool and warm year scenarios. *Prog. Oceanogr.* 197, 1–18, doi:10.1016/j.pocean.2021.102629.
- Danielson, R. E., 2021. On completing a measurement model by symmetry, arXiv:2110.08969 [stat.AP].
- Danielson, R. E., Johannessen, J. A., Quartly, G. D., Rio, M.-H., Collard, F., Chapron, B., Donlon, C., 2018. Exploitation of error correlation in a large analysis validation: GlobCurrent case study. *Remote Sens. Environ.* 217, 476–490, doi:10.1016/j.rse.2018.07.016.
- Danielson, R. E., Zhang, M., Perrie, W. A., 2020. Possible impacts of climate change on fog in the Arctic and subpolar North Atlantic. *Adv. Statist. Clim. Meteor. Ocean.* 475, 1–19, doi:10.5194/ascmo-6-31-2020.
- Dee, D. P., 2005. Bias and data assimilation. *Quart. J. Roy. Meteor. Soc.* 131, 3323–3343, doi:10.1256/qj.05.137.
- DFO, 2020. Whalesightings Database, Team Whale, Fisheries and Oceans Canada, Dartmouth, Nova Scotia [20201202].
- Dong, H., Zhou, M., Hu, Z., Zhang, Z., Zhong, Y., Basedow, S. L., Smith Jr., W. O., 2021. Transport barriers and the retention of *Calanus finmarchicus* on the Lofoten Shelf in early spring. *J. Geophys. Res. Oceans* 126, 1–18, doi:10.1029/2021JC017408.
- Edelmann, D., Móri, T. F., Székely, G. J., 2021. On relationships between the Pearson and the distance correlation coefficients. *Stat. Prob. Lett.* 169, 1–6, doi:10.1016/j.spl.2020.108960.
- Espedal, H. A., Johannessen, O. M., Johannessen, J. A., Dano, E., Lyzenga, D. R., Knulst, J. C., 1998. COASTWATCH’95: ERS 1/2 SAR detection of natural film on the ocean surface. *J. Geophys. Res. Oceans* 103, 24969–24982, doi:10.1029/98JC01660.
- Gavrilchuk, K., Lesage, V., Fortune, S., Trites, A. W., Plourde, S., 2020. A mechanistic approach to predicting suitable foraging habitat for reproductively mature North Atlantic right whales in the Gulf of St. Lawrence. *DFO Can. Sci. Advis. Sec. Res. Doc.* 2020/034. iv + 47p.
- Hamilton, B., Dean, C., Kurata, N., Vella, K., Soloviev, A., Tartar, A., Shivji, M., Matt, S., Perrie, W., Lehner, S., Zhang, B., 2015. Surfactant associated bacteria in the sea surface microlayer: Case studies in the Straits of Florida and the Gulf of Mexico. *Can. J. Remote Sens.* 41, 135–143, doi:10.1080/07038992.2015.1048849.

- Hersbach, H., Bell, B., Berrisford, P., Hirahara, S., Horányi, A., Muñoz-Sabater, J., Nicolas, J., Peubey, C., Radu, R., Schepers, D., Simmons, A., Soci, C., Abdalla, S., Abellan, X., Balsamo, G., Bechtold, P., Biavati, G., Bidlot, J., Bonavita, M., De Chiara, G., Dahlgren, P., Dee, D., Diamantakis, M., Dragani, R., Flemming, J., Forbes, R., Fuentes, M., Geer, A., Haimberger, L., Healy, S., Hogan, R. J., Hólm, E., Janisková, M., Keeley, S., Laloyaux, P., Lopez, P., Lupu, C., Radnoti, G., de Rosnay, P., Rozum, I., Vamborg, F., Villaume, S., Thépaut, J.-N., 2020. The ERA5 global reanalysis. *Quart. J. Roy. Meteor. Soc.* 146, 1999–2049, doi:10.1002/qj.3803.
- Hersbach, H., Stoffelen, A., de Haan, S., 2007. An improved C-band scatterometer ocean geophysical model function: CMOD5. *J. Geophys. Res.* 112, doi:10.1029/2006JC003743.
- Kenney, R. D., 2019. The North Atlantic Right Whale Consortium database: A guide for users and contributors (accessed January 2021 at https://www.narwc.org/uploads/1/1/6/6/116623219/narwc_users_guide_v.6_.pdf).
- Kenney, R. D., Mayo, C. A., Winn, H. E., 2001. Migration and foraging strategies at varying spatial scales in western North Atlantic right whales: A review of hypotheses. *J. Cetacean Res. Manage.* (special issue) 2, 251–260, doi:10.47536/jcrm.vi.283.
- Koch, W., 2004. Directional analysis of sar images aiming at wind direction. *IEEE Trans. Geosci. Remote Sens.* 42, doi:10.1109/TGRS.2003.818811.
- Koutitonsky, V. G., Bugden, G. L., 1991. The physical oceanography of the Gulf of St. Lawrence: A review with emphasis on the synoptic variability of the motion, p. 57-90. *The Gulf of St. Lawrence: Small ocean or big estuary?* Can. Spec. Publ. Fish. Aquat. Sci., 113.
- Kudryavtsev, V., Akimov, D., Johannessen, J., Chapron, B., 2005. On radar imaging of current features: 1. Model and comparison with observations. *J. Geophys. Res.* 110, 1–27, doi:10.1029/2004JC002505.
- Kudryavtsev, V., Myasoedov, A., Chapron, B., Johannessen, J. A., Collard, F., 2012a. Imaging mesoscale upper ocean dynamics using synthetic aperture radar and optical data. *J. Geophys. Res.* 117, doi:10.1029/2011JC007492.
- Kudryavtsev, V., Myasoedov, A., Chapron, B., Johannessen, J. A., Collard, F., 2012b. Joint sun-glitter and radar imagery of surface slicks. *Remote Sens. Environ.* 120, 123–132, doi:10.1016/j.rse.2011.06.029.
- Kurata, N., Vella, K., Hamilton, B., Shivji, M., Soloviev, A., Matt, S., Tartar, A., Perrie, W., 2016. Surfactant-associated bacteria in the near-surface layer of the ocean. *Sci. Rep.* 6, 19123, doi:10.1038/srep19123.
- Lavoie, D., Simard, J. C. Y., Lambert, N., Galbraith, P. S., Roy, N., Brickman, D., 2016. Large-scale atmospheric and oceanic control on krill transport into the St. Lawrence Estuary evidenced with three-dimensional numerical modelling. *Atmos.–Ocean* 54, 299–325, doi:10.1080/07055900.2015.1082965.
- Maps, F., Plourde, S., McQuinn, I. H., St. Onge-Drouin, S., Lavoie, D., Chassé, J., Lesage, V., 2015. Linking acoustics and finite-time Lyapunov exponents reveals areas and mechanisms of krill aggregation within the Gulf of St. Lawrence, eastern Canada. *Limnol. Oceanogr.* 60, 1965–1975, doi:10.1002/lno.10145.
- Munk, W., Armi, L., Fischer, K., Zachariasen, F., 2000. Spirals on the sea. *Proc. Roy. Soc. Lond. A* 456, 1217–1280.
- NARWC, 2021. Identification and Sightings Data of the North Atlantic Right Whale Consortium as of January 2021 (offline archive at New England Aquarium, Boston, Massachusetts, U.S.A.).
- Peacock, T., Haller, G., 2013. Lagrangian coherent structures: The hidden skeleton of fluid flows. *Phys. Today* 66, 41–47, doi:10.1063/PT.3.1886.
- Plourde, S., Lehoux, C., Johnson, C. L., Perrin, G., Lesage, V., 2019. North Atlantic right whale (*Eubalaena glacialis*) and its food: (I) a spatial climatology of *Calanus* biomass and potential foraging habitats in Canadian waters. *J. Plankton Res.* 41, 667–685, doi:10.1093/plankt/fbz024.

- Raschle, N., Chapron, B., Ponte, A., Ardhuin, F., Klein, P., 2014. Surface roughness imaging of currents shows divergence and strain in the wind direction. *J. Phys. Oceanogr.* 44, 2153–2163, doi:10.1175/JPO-D-13-0278.1.
- Sorochan, K., Plourde, S., Morse, R., Pepin, P., Runge, J., Thompson, C., Johnson, C. L., 2019. North Atlantic right whale (*Eubalaena glacialis*) and its food: (II) interannual variations in biomass of *Calanus spp.* on western North Atlantic shelves. *J. Plankton Res.* 41, 687–708, doi:10.1093/plankt/fbz044.
- Sorochan, K. A., Plourde, S., Baumgartner, M. F., Johnson, C. L., 2021. Availability, supply, and aggregation of prey (*Calanus spp.*) in foraging areas of the North Atlantic right whale (*Eubalaena glacialis*). *ICES J. Mar. Sci.* 78, doi:10.1093/icesjms/fsab200.
- Székely, G. J., Rizzo, M. L., 2009. Brownian distance covariance. *Annals of Applied Statistics* 3, 1236–1265, doi:10.1214/09-AOAS312.
- Székely, G. J., Rizzo, M. L., Bakirov, N. K., 2007. Measuring and testing dependence by correlation of distances. *Annals of Statistics* 35, 2769–2794, doi:10.1214/009053607000000505.
- Young, G., Sikora, T., Winstead, N., 2008. Mesoscale near-surface wind speed variability mapping with synthetic aperture radar. *Sensors* 8, 7012–7034, doi:10.3390/s8117012.
- Zhang, B., Perrie, W., He, Y., 2011. Wind speed retrieval from RADARSAT-2 quad-polarization images using a new polarization ratio model. *J. Geophys. Res.* 116, 1–13, doi:10.1029/2010JC006522.